JOURNAL OF MATERIALS SCIENCE **36** (2001) 5811–5821

Superplastic flow in nanocrystalline and sub-microcrystalline yttria-stabilized tetragonal zirconia

U. BETZ
Institute for Materials Science, Thin Films Division, Darmstadt University of Technology, Petersenstr. 23, 64287 Darmstadt, Germany

K. A. PADMANABHAN*
Institute of Nanotechnology, Research Center for Technology and Environment, P.O. Box 3640, D-76021 Karlsruhe, Germany
E-mail: office@int.fzk.de

H. HAHN
Institute for Materials Science, Thin Films Division, Darmstadt University of Technology, Petersenstr. 23, 64287 Darmstadt, Germany

Tensile deformation of nanocrystalline $ZrO_2 + 5$ mol% Y_2O_3 at temperatures in the range of 1283–1403 K is described. It is demonstrated (a) that steady state flow is possible at temperatures of the order of 0.42 T_m, where T_m is the absolute melting point, (b) that 70% engineering strain could be obtained at 1403 K (0.46 T_m), and (c) that significant grain boundary sliding was present during deformation. Static and dynamic grain growth as also a decrease in the relative density of the specimen with deformation could be observed. The present results as well as those of Owen and Chokshi concerning superplastic flow in sub-microcrystalline materials taken from literature could be accounted for quantitatively using the grain boundary sliding controlled flow model of Padmanabhan and Schlipf, originally proposed for microcrystalline superplastic alloys.

1. Introduction

Superplastic flow in metallic materials was established in the early years of the twentieth century [1–3]. Starting from 1985, this phenomenon has also been demonstrated in ceramic materials, one of the most extensively studied systems being yttria-doped partially stabilized tetragonal zirconia [4–14]. Almost from the beginning, it was realized that grain/interphase boundary sliding is the dominant process in superplastic deformation. In 1971 this mode of deformation was identified for the first time as the mechanism *controlling* the rate of optimal superplastic flow [15–17]. A divergent view has also existed all along that boundary sliding is an inherently fast process and that only diffusion or dislocation slip can control the rate of flow [1–3, 18–21].

More recently, it has been realized that the net contribution of dislocation slip to external superplastic strain is zero [22]. This mechanism as a rate controlling process becomes even less attractive for submicrocrystalline and nanocrystalline materials in which also superplastic behavior is seen [23–25]. Nor is it of much relevance in understanding superplastic flow in ceramic materials.

Diffusion and grain boundary sliding are interdependent processes and the slower of the two determines the overall rate of deformation [26, 27]. Thus, even in diffusion controlled flow grain boundary sliding is present. But here the latter process is considered to be faster than the former. There is clear evidence for the occurrence of grain boundary sliding during superplastic deformation in both metallic and ceramic materials (see below also). A fully consistent model can be constructed by treating either diffusion or grain boundary sliding to be rate controlling [28]. But, considering grain boundary sliding to be rate controlling has the following advantages: (a) The significant near-random grain rotations present during superplastic flow can be quantitatively accounted for [29, 30]. (b) Aided by boundary migration [31, 32], this process can easily explain why the grain shape remains practically unchanged even after extreme elongation. (c) The analysis applies equally to metallic *and* ceramic superplastics. (d) Recently, the analysis has been extended to explain the deformation of nanostructured materials also [23, 24].

Using experimental data pertaining to a number of systems, the model has been shown to describe

*Author to whom all correspondence should be addressed.

accurately superplastic flow in microcrystalline- and nanocrystalline- materials [23, 25, 33, 34]. In this paper, the first set of detailed results pertaining to tensile (superplastic) deformation behavior of nanocrystalline yttria doped partially stabilized zirconia (n-Y-PSZ) is reported at temperatures below 0.5 Tm. It is also shown that these results as well as the earlier ones on submicrocrystalline yttria stabilized tetragonal zirconia (Y-TZP) [13] are consistent with the model in which grain/interphase boundary sliding is regarded as the rate controlling process [23, 25, 28].

2. The model

A full description is available elsewhere [23–25, 28, 30–34]. Only those aspects of the model needed for this paper are discussed here.

2.1. Theory

It is assumed that rate controlling flow is confined to a network of deforming grain- and interphase-boundaries that surround essentially non-deforming grains except for what is required to achieve strain and geometric compatibility [28]. Boundaries of high viscosity can be bypassed by grain rotation [29, 30]. In the analysis, a boundary is divided into a number of atomic scale ensembles ("basic units" of sliding) that contain free volume [35]. For calculations, the basic unit is assumed to be an oblate spheroid of ground area $\pi\delta^2$ in the boundary plane and radius on either side of the boundary of $(\delta/2)$, where δ is the grain boundary width. At a high homologous temperature most of the energy of activation is available from thermal energy. Then, the basic unit can shear to a neighboring configuration if the shear stress exceeds $\tau_i (= \Delta F_i/\gamma_i V_0)$, where ΔF_i is the free energy of the shear transformation, γ_i the strain associated with the unit shear event and $V_0 = 2/3\ \pi\delta^3$ is the volume of the basic unit.

According to Wolf [35] the excess free volume of high angle grain boundaries varies only slightly with misorientation. This has two consequences. First, for stresses $\tau \geq \tau_i$ the configuration C′ is topologically equivalent to C_{eq} (equilibrium configuration) and forms the new equilibrium configuration C'_{eq}. Again there will be metastable states C″ nearby, which are transformed by the action of τ_i to a lower energy state of C''_{eq} equal to C_{eq} so that grain boundary sliding can proceed by a sequence of shear transformations. The equivalence of C_{eq} and C'_{eq} constitutes isoconfigurational flow kinetics which can be described by transition state theory [28]. Second, the individual shear transformations γ_i and the accompanying transient volume expansions ε_i as the basic unit shears in an embedded solid matrix will not differ much for different basic units or for the different metastable states within a basic unit. Thus γ_i and ε_i can be replaced by their averages γ_0 and ε_0 respectively. The values of ΔF_i, however, will vary because the shear distortions will partly remain, depending on the state of deformation of the neighborhood. This spectrum of activation energy values will be centred around a mean value ΔF_0, which corresponds to a shear transformation of γ_0 and a transient volume expansion ε_0. (In other words, the elastic energy of the shear and transient volumetric distortions constitutes the free energy of transformation, ΔF_0, for the boundary sliding process involving a basic unit.).

In high temperature creep, steric hindrance makes this atomic scale sliding rather ineffective and causes triple point cracking and premature failure. In order to produce substantial sliding on a mesoscopic scale (defined to be of the order of a grain diameter or more), two or more grain boundaries must cooperate to form a plane interface which by interconnection with other similar plane interfaces enables long range sliding until stopped by an insurmountable barrier, e.g., an extra large grain or a coarse precipitate. The driving force for plane interface formation is the reduction in the overall grain boundary energy through a reduction in the grain boundary area in the direction of sliding and this is achieved through local boundary migration [28, 31]. (This is a much easier process than that envisaged in diffusion models in which diffusion distances of the order of the grain size are involved.)

Thus, in this approach grain/interface boundary sliding is visualized as a two scale phenomenon. On the microscopic scale the obstacles to sliding are localized and can be overcome by thermal activation. Short range internal stresses develop at this level. On a mesoscopic scale the obstacles to sliding are other grains or particles residing at grain/interphase boundaries. The internal stresses associated with sliding at this level have a long range and manifest themselves as a threshold stress (which should be substracted from the applied stress to know the effective stress driving the microscopic scale sliding process).

The threshold stress, σ_0, needed to be overcome before a plane interface that allows mesoscopic sliding can form is estimated as follows. At the mesoscopic level, the polycrystalline structure is described as a cubic dense packing of equisized spheres. The walls of the Wigner-Seitz cell containing one sphere represent the grain boundaries. This corresponds to a face centered cubic structure on a mesoscopic scale with glide planes and glide directions. Since the roughness is the lowest on the {111} planes, these are assumed to be the glide planes for long range (mesoscopic) sliding. In order to create a plane interface, the peaks and troughs of the mesoscopic {111} plane must be removed by local migration. For this to happen, the grain boundary area perpendicular to the plane interface will have to increase by an amount ΔA per grain. (However, in view of the decrease in grain boundary area in the direction of sliding the net change in grain boundary area is negative [28].) The number of grain boundaries, N, that participate in such a mesoscopic sliding event can be calculated theoretically by minimizing the energy expenditure per grain as a function of N. This is yet to be done. So, at present N is experimentally determined using scanning/transmission electron microscopy (see, Figs 4 and 6 of ref. [31]).

Mathematical development of the above ideas for a grain of average size D, rhombic dodecahedral shape and specific grain boundary energy γ_B in a material of

shear modulus G, leads to an expression [28, 33]

$$\sigma_0 = 3^{0.5}\left(\frac{2G\gamma_B}{\alpha_f}\right)^{0.5}\left[\frac{\Delta A/A}{(NA)^{0.5}}\right]^{a_2} \quad (1)$$

where α_f is a form factor of the order of unity and A is the grain boundary area per grain.

For a single phase material of uniform grain size, $a_2 = 0.5$. In real materials 'a_2' will depend on the grain size and shape distributions, as well as the ratio of phases, subject to the constraint $0 < a_2 \leq 0.5$. G, γ_B and N are material properties known/determined from experiments. From the geometry of rhombic dodecahedron,

$$\Delta A = \left(\frac{2^{0.5}}{8}D^2\right) \quad \text{and} \quad A = \left[\frac{3^{0.5}}{4}D^2\right].$$

As stated above, an effective stress $\sigma_{\text{eff}} = (\sigma - \sigma_0)$ will be available for the atomic scale (microscopic) sliding process. The rate equation is obtained as [28, 33, 34]

$$\dot{\varepsilon} = \left(\frac{\delta}{3^{0.5}}\frac{\gamma_0^2 V_0 \omega_0}{DkT\sigma_m}\right)\left[(\sigma - \sigma_0)\{\sigma_m + \alpha(\sigma - \sigma_0 - 2\sigma_m)\} + \sigma_m^2\,\alpha\exp\left(-\frac{1}{\alpha}\right)\right] \quad (2)$$

where $\omega_0 = \nu\exp(-\Delta F_0/kT)$, with ν the thermal vibration frequency. k is the Boltzmann constant, $\Delta F_0 (= Q - T\,\Delta S)$ the free energy of the unit sliding event, Q the activation energy for the rate controlling process, T the absolute temperature of deformation and ΔS is the entropy of activation. σ_m and $\lambda (= 2/\alpha\pi^{0.5})$ are the mean and the standard deviation of the internal stress distribution at a boundary arising from (atomic scale) sliding.† From bubble raft experiments $\gamma_0 \cong 0.1$ and field ion microscopy has revealed that in many materials $\delta \cong 2.5b$, where b is the average interatomic spacing in the boundary region. ΔF_0 can be calculated *ab initio* from the Eshelby relationship [28, 33]

$$\Delta F_0 = \frac{1}{2}\left(\beta_1\gamma_0^2 + \beta_2\varepsilon_0^2\right)GV_0 \quad (3)$$

where $\beta_1 = 0.470(1.590 - p)/(1 - p)$, $\beta_2 = 4(1 + p)/[9(1 - p)]$, with p the Poisson ratio and the tensile strain resulting from unit shear $\varepsilon_0 \cong (\gamma_0/2) = 0.05$.

2.2. Numerical validation

Equation 2 can be rewritten as

$$\dot{\varepsilon} = a\sigma^2 + b\sigma + c \quad (4)$$

†Equation 2 is obtained as a linear approximation ($\sigma - \sigma_0 = \sigma' \cong \sigma_m + u$) of the rigorous equation [28]

$$\dot{\varepsilon} = \frac{\delta\gamma_0^2 V_0\omega_0}{3^{0.5}DkT}\left\{\sigma'\left[1 + \alpha\left(\ln\frac{\sigma'}{\sigma_m} - 1\right)\right] + \sigma_m\,\alpha\exp\left(-\frac{1}{\alpha}\right)\right\};$$
$$\sigma' = (\sigma - \sigma_0)$$

The dimensional consistency of this equation is evident when it is realized that $(\gamma_0^2 V_0)$ has the dimensions of (energy/G) (since strain = (stress/G); stress × strain × volume = energy).

where

$$a = \left(\frac{\alpha C_1}{\sigma_m}\right), \quad \text{with} \quad C_1 = \left(\frac{1}{3^{0.5}}\frac{\delta}{D}\frac{\gamma_0^2 V_0\omega_0}{kT}\right);$$
$$b = \left(\frac{C_1}{\sigma_m}\right)[\sigma_m - 2\alpha\sigma_0 - 2\alpha\sigma_m];$$
$$c = \left(\frac{C_1}{\sigma_m}\right)\left[\alpha\sigma_0^2 + 2\alpha\sigma_0\sigma_m - \sigma_0\sigma_m + \sigma_m^2\,\alpha\exp\left(-\frac{1}{\alpha}\right)\right] \quad (5)$$

The 'best fit estimates' of the constants a, b, c ($a > 0$, $b > 0$, $c < 0$ [34]) in Equation 4 can be obtained unambiguously by a least squares analysis. From Equation 5

$$\sigma_m^2 = \frac{1}{4a^2}\frac{(b^2 - 4ac)}{\left(\frac{1}{2\alpha} - 1\right)^2 - \exp\left(-\frac{1}{\alpha}\right)} \quad (6)$$

$$\sigma_0 = \sigma_m\left(\frac{1}{2\alpha} - 1\right) - \frac{b}{2a} \quad (7)$$

$$C_1 = (a\sigma_m/\alpha) \quad (8)$$

From Equation 6, $0 < \alpha \leq \alpha_c \cong 0.390$ [34]. In addition to Equations 6–8, a fourth condition is introduced through the statistical criterion of 'minimum variance unbiased estimate', i.e., in the best solution the standard deviation is a minimum (or $\alpha = 2/(\lambda\pi^{0.5})$ is a maximum).

From the physical nature of the problem [33, 34]

$$\sigma_0 < \sigma_{\min} = \min_{i=1,2,\ldots,N}\{\sigma_i\};$$
$$\sigma_m < \sigma_{\max} = \max_{i=1,2,\ldots,N}\{\sigma_i\}; \quad (9)$$

where $\{\sigma_i\}$ represents the set of experimental values used to estimate a, b, c. Thus α is increased from 0 to its limiting value of 0.390 in steps of 0.001 (say) and using this value of α, for each case σ_m, σ_0, and C_1 values are calculated from Equations 6–8. The highest value of α for which the inequalities in Equation 9 are satisfied is accepted as the final answer and the corresponding $\alpha, \sigma_m, \sigma_0, C_1$ values are taken as the constants of the physical model. Thus, in this analysis at the macrolevel the stress-strain rate data can be accounted for using three constants. If the material properties G, γ_B, p, δ, N and γ_0 are known from literature or separate experiments, these three constants of the constitutive equation can be calculated *ab initio*.

2.3. Grain size dependence of strain rate

From Equation 1 and the expressions for ΔA and A given below that equation, it follows that $\sigma_0 \propto 1/D^{a_2}$. '$a_2$' is determined as follows: from Equations 4–9, the 'best estimate' of σ_0 is obtained (Equation 7) for different grain sizes. From these results 'a_2' is obtained by a least squares analysis using the relationship $\sigma_0 = \frac{K_1'}{D^{a_2}}$, where K_1' is a constant (equal to $[6^{0.5}\cdot(\frac{2}{3})^{0.5a_2}(G\gamma_B)^{0.5}(\frac{1}{\alpha_f N^{0.5}3^{0.25}})^{a_2}]$. Substituting this grain size dependence in Equation 2, the grain size dependence of strain rate for the model is obtained as

$$\ln \dot{\varepsilon}_\sigma \cong A_1 - \ln D - \frac{A_2}{D^{a_2}} + \frac{A_3}{D^{2a_2}} \qquad (10)$$

where A_1, A_2, A_3 are constants that have absorbed all other constants. (Equation 10 has been derived here for the first time by truncating an infinite series expansion for the logarithmic function on the right hand side at the second degree.) The suffix (σ) denotes the variable that is kept constant.

2.4. Activation energy for the rate controlling process

From Equation 5

$$C_1 = B_0\left(\frac{\nu}{kT}\right)\exp\left(-\frac{Q}{RT}\right) \qquad (11)$$

where B_0 has absorbed the other constants [34]. The thermal vibration frequency, ν, is taken either as equal to (kT/h) or as $10^{13}\ s^{-1}$ (h is Planck's constant). It has already been shown that the difference in the activation energy for the rate controlling process, Q, obtained by using either of these two values is rather small [33, 34]. Therefore, in the present calculations ν is taken as equal to (kT/h). Then,

$$C_1 = B_1\exp\left(-\frac{Q}{RT}\right) \qquad (12)$$

with $B_1 = (B_0/h)$. Thus, Q can be evaluated from Equation 12 by plotting $\ln C_1$ values corresponding to different temperatures against $1/T$.

3. Experimental

Nanocrystalline oxide powders of ZrO_2 and Y_2O_3 were synthesized using the inert gas condensation (IGC) technique [36]. Zirconium monoxide and yttrium metal were evaporated separately in a helium atmosphere at an initial pressure of 2 mbar. The small particles formed above the tungsten crucible due to the condensation of the vapor phase in the helium atmosphere were quickly transported through the growth zone by gas convection and deposited as loose powder by thermophoretic forces on a stainless steel plate kept at liquid nitrogen temperature. To obtain stoichiometric ZrO_2 and Y_2O_3, an oxygen atmosphere was introduced in the IGC chamber once the evaporation process was complete. After collection of the powder particles from the cold plate a further oxidation step of annealing in a flowing oxygen atmosphere at 573 K for 2 hours was resorted to. By pre-mixing the dry powders and suspending them in alcohol, a composition of $ZrO_2 + 5$ mol% Y_2O_3 was obtained. The suspension was ultrasonically vibrated and simultaneously stirred. Following drying and crushing, the powders were compacted at room temperature by applying a uniaxial pressure of 80 MPa. Then, cold isostatic pressing at a maximum pressure of 460 MPa was employed. Ceramic discs of about 28 mm diameter and 2 mm thickness were obtained using pressureless sintering at 1423 K for 2 hours in vacuum. To ensure/re-establish stoichiometric composition, cooling to room temperature was done in flowing oxygen. The heating as well as the cooling rate was maintained at 200 Kh^{-1}. (It is evident that the method of preparation of dense, truly nanocrystalline ceramic samples is rather time consuming. This explains the near-total absence of tensile deformation data for this class of materials.)

The ceramic discs were machined using diamond coated tools to obtain dog-bone shaped tensile specimens of gauge length 10.0 mm, thickness of about 1.5 mm and width 2.5 mm. The pieces left from cutting were used as reference samples. Properly located holes were placed in the grip region for mounting the specimens on to the testing machine. Al_2O_3 pins and Al_2O_3 pull rods were used for this purpose. The test assembly was surrounded by a furnace of dimensions 100 mm diameter and 250 mm height. It was fitted with 6 silicon carbide heating elements. The maximum attainable temperature was 1773 K. Using a microprocessor based program controller and a Pt/Pt-Rh 13% R-type thermocouple, an accuracy of ± 1 K could be ensured in the tensile tests. Exact temperature determination on the tensile specimen (between the alumina pull-rods) was made using Philips temperature control rings. The specimen/test assembly was heated from room temperature to the test temperature. Apart from the tensile specimen a reference piece from the same ceramic disc (of identical initial microstructure) was placed at the top of the lower pull-rod and it experienced the same thermal treatment as the test specimen.

A closed loop servohydraulic MTS machine (model 810.12) of 10 ton capacity was used for the tensile tests. The full capacity of the load cell was 100 kg, but the present experiments were done in the 10% range of that load cell. All tests were in air in the stroke control mode, i.e., the rate of cross-head displacement was kept constant.

Specific surface areas of the nanocrystalline powders and powder compacts were calculated from N_2-adsorption measurements applying multipoint BET (Brunauer, Emmett, Teller) analysis. Pore size distributions of the channel-like-open porosity of nanocrystalline green bodies were evaluated from the desorption branch of the N_2-adsorption isotherm using the BJH (Barrett, Joyner, Hallenda) theory.

Grain sizes of powders, compacts and ceramic discs were calculated from the broadening of the XRD peaks using the Scherrer formula. These values were then cross-checked by high resolution scanning electron microscopy (HRSEM). Tensile tested specimens were also subjected to standard scanning electron microscopy. Relative densities of specimens were determined by the Archimedes principle (immersion in water). After each step, including sintering and deformation, crystal structure was identified by comparing the peak positions in the XRD patterns of the present samples with those published in literature.

In addition to the present results, data presented by Owen and Chokshi [13] were also analyzed in terms of the grain/interphase boundary sliding controlled flow model presented in Section 2 to establish that the model, earlier shown to be valid for microcrystalline materials, is also useful for understanding tensile flow in submicrocrystalline and nanocrystalline materials.

4. New results

The starting nanocrystalline (n-) zirconia powders had monoclinic and tetragonal phases of average grain size 8 nm. The specific surface area was 120 $m^2\,g^{-1}$. The yttria powders had a monoclinic structure, an average grain size of 14 nm and a specific surface area of 60 $m^2\,g^{-1}$. Absence of hysteresis between the adsorption and desorption branches of the isotherms of nitrogen adsorption measurements in both the powders revealed that the powders were rather loosely agglomerated.

Room temperature (green) compacts of $ZrO_2 +$ 5 mol% Y_2O_3 had a relative density of 40%. After compaction, the tetragonal phase was absent and only the monoclinic phase was observed in zirconia. The crystallographic structure of yttria was retained. The specific surface area of the green compact was 99.8 $m^2\,g^{-1}$. The pore size distribution was lognormal and the average pore diameter 8 nm. After sintering, the tetragonal and the cubic phases were stabilized with a tetragonal phase content $X_{tet} \approx 70\%$. The relative density of the sintered discs ranged between 84 and 94%. The average grain size varied between 45 and 75 nm.

At 1283 K ($0.42T_m$, where T_m is the absolute melting temperature of zirconia), a specimen of average grain size of 54 nm was subjected to an engineering strain of 0.08 at an initial strain rate of $5.7 \times 10^{-6}\,s^{-1}$. To the best of our knowledge, this is the lowest temperature to date at which yttria partially stabilized zirconia has been deformed into the steady state. The largest elongation in the present experiments, which was about 70% engineering strain, was obtained at 1403 K ($0.46T_m$) in a specimen of initial grain size 75 nm and density 94% of theoretical value deformed at an initial strain rate of $3.1 \times 10^{-5}\,s^{-1}$. The true (flow) stress - true strain curves of both the samples are presented in Fig. 1. (Evidently, in both cases steady state flow got established.) Fig. 2 displays an untested sample, along with the specimen that experienced the maximum elongation at 1403K—a temperature normally considered to be low for the deformation of $ZrO_2 + 5$ mol%Y_2O_3. The deformation in the gauge portion of the specimen

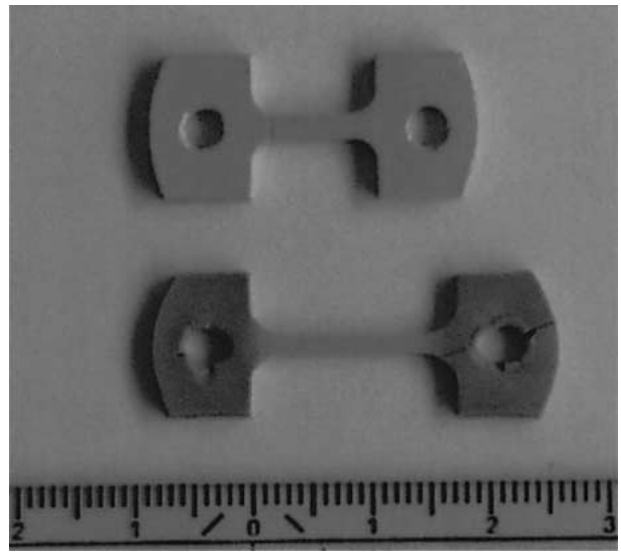

Figure 2 Photograph of dog-bone shaped tensile samples with a sample showing the original dimensions (above) and another homogeneously elongated specimen (below). An engineering strain of more than 70% could be obtained in this nanocrystalline material at 1403 K.

was homogeneous; the cracks at the holes developed when the specimen was being removed from the test assembly (very tight gripping by the assembly pins following heating). Fracture started at machining marks left on the specimen surface due to inadequate polishing. Thus the 70% elongation obtained may be regarded as a conservative value.

Using sub-microcrystalline (grain size $\approx$ 300 nm) zirconia powder, elongations of several hundred percent have been obtained at 1823K [3]. But this is the first report of substantial elongation (70%) in a truly nanocrystalline material (grain size less than 100 nm) prepared by the powder metallurgy route and tested at a homologous temperature of $0.46T_m$. In the sub-microcrystalline material an elongation of 60% could be obtained at 1473 K ($0.49T_m$). Flow behavior was investigated in detail at a temperature of 1333 K ($0.44T_m$). In Fig. 3 the flow stress is plotted as a function of true strain corresponding to five different cross-head speeds (the initial strain rates are indicated

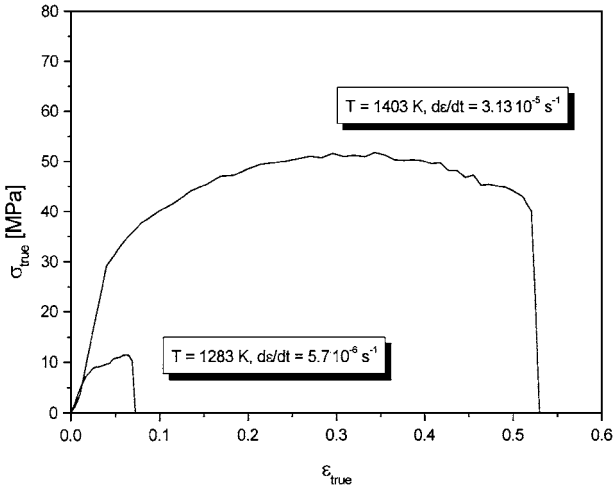

Figure 1 True flow stress as a function of true strain for two nanocrystalline 5Y-PSZ samples tested at 1283 K and at 1403 K at initial strain rates of $3.1 \times 10^{-5}\,s^{-1}$ and $5.7 \times 10^{-6}\,s^{-1}$, respectively.

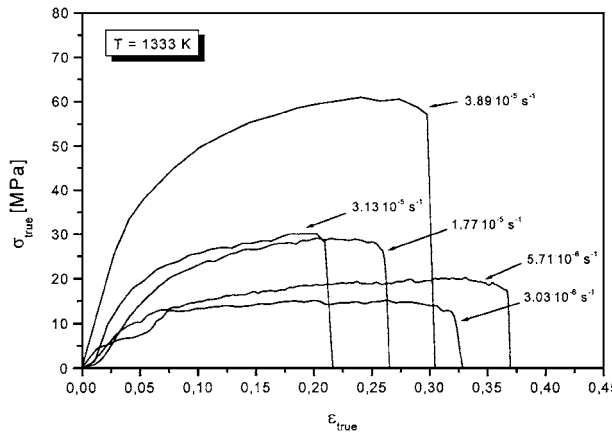

Figure 3 True flow stress as a function of true strain for different nanocrystalline 5Y-PSZ samples tested under constant cross-head speed conditions in the range of $3 \times 10^{-6}\,s^{-1}$ to $3.9 \times 10^{-5}\,s^{-1}$ at a temperature of 1333 K.

in the figure). In all cases steady state flow was present and flow stress increased with strain rate. Initial values of the relative density, ρ_{rel}, and the average grain size, D_0, of the samples were $85 \pm 1\%$ and 50 ± 5 nm, respectively.

No (or negligible) change in the contents of the phases present (tetragonal and cubic) was noticed after the deformation. In all cases the grain size of the reference sample that was exposed to temperature for the duration of the test was greater than the starting grain size. The grain size in the gauge portion of the specimen that was exposed to both temperature and strain was greater than that in the reference sample. Thus, static grain growth could be separated from dynamic grain growth. It was also seen that exposure to temperature had increased the relative density of the reference sample but deformation had caused a decrease in the relative density in the gauge portion. (Therefore, plots like Figs 1 and 3, which assume constant volume, are approximate.) For example, in a specimen of initial grain size of 75 nm tested at 1403 K for 7 hours, an engineering strain of 70% was obtained. During this period, the average grain size in the reference sample had increased to 95 nm but that in the gauge portion was 128 nm. The relative density of the starting specimen was 94%, which had increased to 96% in the reference sample but had fallen to 92% in the gauge portion.

In tested specimens, regions away from the fracture zone were dense and contained equiaxed grains. (A high resolution SEM picture is presented and discussed in the next section.) Similar to what was seen in metallic specimens undergoing high temperature (superplastic) deformation, grain boundary sliding started at boundaries that were inclined favourably to the stress axis. In view of the limited ductility of the present ceramic material compared with metallic alloys, cavitation and cracking developed throughout the specimen rather early (Fig. 4a) Loss of density mainly arose due to cracks that developed perpendicular to the tensile axis. These cracks originated at surface flaws left after polishing, e.g., grinding lines perpendicular to the tensile axis. Void nucleation was preferentially present at triple junctions of grains. Cracks several hundred micrometers long were observed on the surface of deformed samples. A careful examination further revealed that the onset of cracking depended critically on the efficiency of compacting and sintering as well as the degree of polishing of the specimen prior to testing (Fig. 4b). It is well known that the distribution and morphology of the voids and cracks have a strong bearing on the magnitude of the strain to fracture. A quantitative investigation has been planned for the future.

5. Discussion

5.1. New results

In all samples tested at 1333 K ($\rho_{rel} = 85 \pm 1\%$; $D_0 = 50 \pm 5$ nm) steady state had set in at a true strain of 0.15. The stress-strain rate data at this strain are presented in Fig. 5 and analyzed in terms of the simple two parameter power law $\dot{\varepsilon} = K_1 \sigma^n$, with K_1 and n (stress exponent) empirical constants ($n = 1/m$, with m the strain rate sensitivity index), and the atomistic model for grain boundary sliding controlled flow (Equation 4). For the two parameter power law a constant strain rate sensitivity index of 0.41 was determined, whereas in case of the atomistic model m increased from 0.27 at the lowest instantaneous strain rate value of $2.6 \times 10^{-6}\ s^{-1}$ to 0.48 at the highest value of $3.3 \times 10^{-5}\ s^{-1}$ (calculated from the slope of the theoretical curve). On the basis of a χ^2-minimization fit, the boundary sliding controlled flow model resulted in a slightly lower value of χ^2. Since the power law model does not provide for a change in the m-value, it is anticipated that the difference between the two models will become more pronounced over a larger range of strain rates. In the present experiments, due to difficulties in sample preparation in large quantities, the strain rate could only be varied over one order of magnitude. This strain rate range has to be extended to clearly establish the superiority of Equation 4 over the two parameter power law. For the present results both the equations predict acceptable levels of accuracy; but the model for grain boundary sliding controlled flow results in a somewhat better fit with the experimental data.

Taking the experimental strain rate ($\dot{\varepsilon}$)- stress (σ) values presented in Fig. 5, Equations 4–8 and the minimum variance unbiased estimate criterion, the $\alpha, C_1, \sigma_0, \sigma_m$ values were evaluated for the present results as 0.308, $1.81 \times 10^{-6} MPa^{-1}\ s^{-1}$, 12 MPa and 56 MPa respectively. Using these values, it could be ensured that the observed strain rates of deformation could be predicted at different stress levels very accurately. (In microcrystalline materials tested over a wide range of strain rates, it has already been shown that Equation (4) is preferable to the two parameter power law [34].)

For the experimental points at 1333 K, the following phenomenological expression for dynamic grain growth was obtained by a least squares analysis (Fig. 6a):

$$\frac{dD_{dyn}}{dt} = \gamma \cdot D_{dyn} \cdot \left(\frac{d\varepsilon}{dt}\right)^f \qquad (13)$$

with $\gamma = 1.01$ and $f = 1.03$. A relationship of this kind has also been reported for microcrystalline 3Y-TZP [37], where $\gamma = 0.13$ and $f = 0.97$. Theoretical approaches to dynamic grain growth [38–41] differ in physical details (diffusion or dislocation motion) but the mathematical formulations are similar to Equation 13. In these models a linear dependence between dynamic grain growth rate and strain rate is predicted ($f = 1$). γ is a constant that depends on both the mechanism and the material. Therefore, based on the phenomenological Equation 13 no further discussion is possible on the physical mechanism controlling dynamic grain growth.

In Fig. 6b a linear increase in the normalized density loss rate versus strain rate divided by time is obtained in a double logarithmic plot ($T = 1333$ K). The following least squares relation was valid:

$$\frac{d\rho_{dyn}}{dt} = \kappa \cdot \rho \cdot \left(\frac{1}{t} \cdot \frac{d\varepsilon}{dt}\right)^\varphi \qquad (14)$$

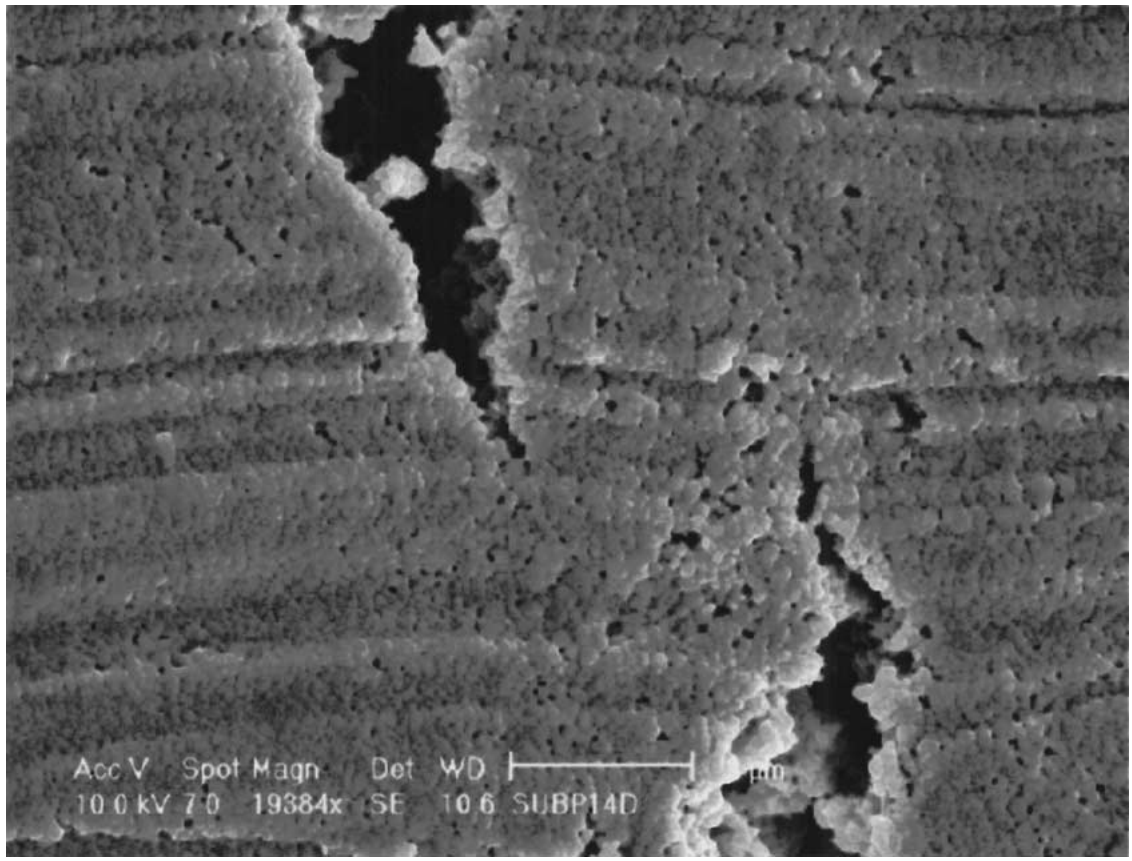

(a)

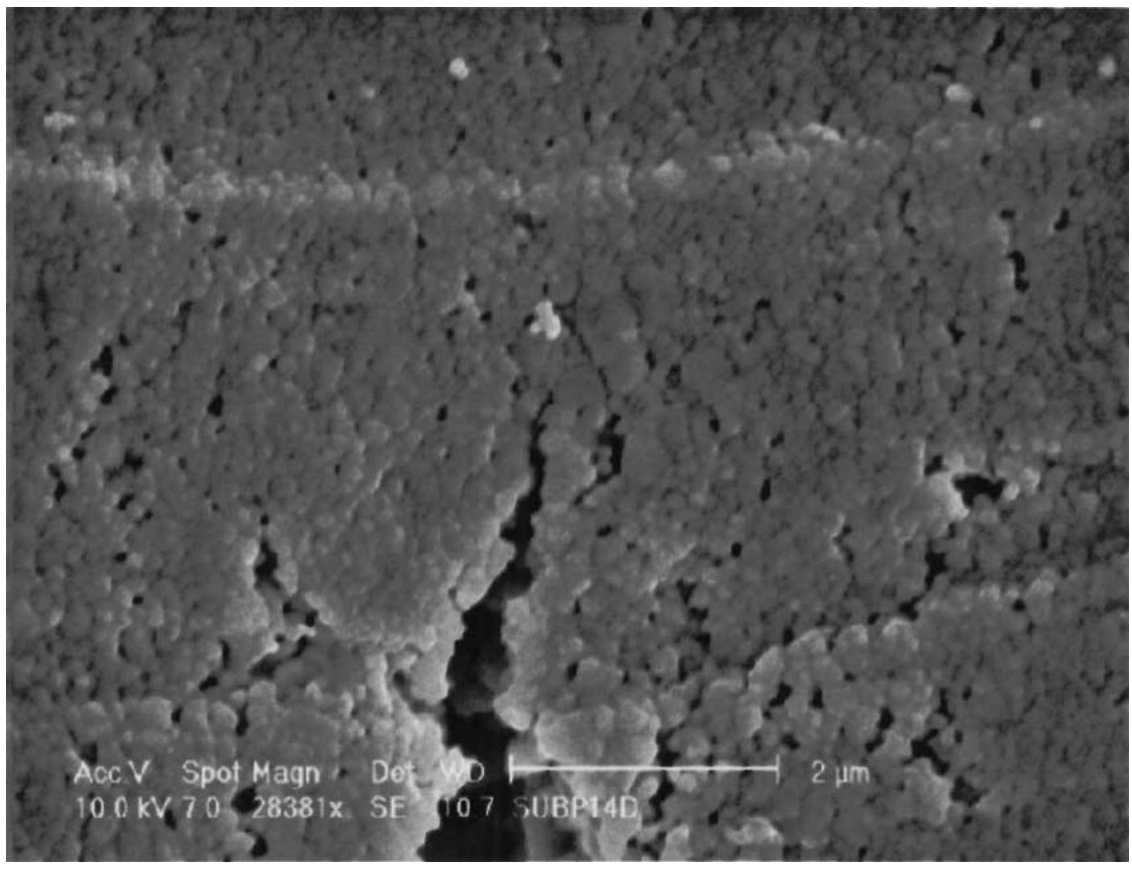

(b)

Figure 4 (a) Cracking along boundaries that experienced maximum deformation; (b) evidence for cracking all over the specimen which could be traced to problems associated with compacting, sintering and polishing of specimen prior to testing (test temperature 1333 K; elongation 16%).

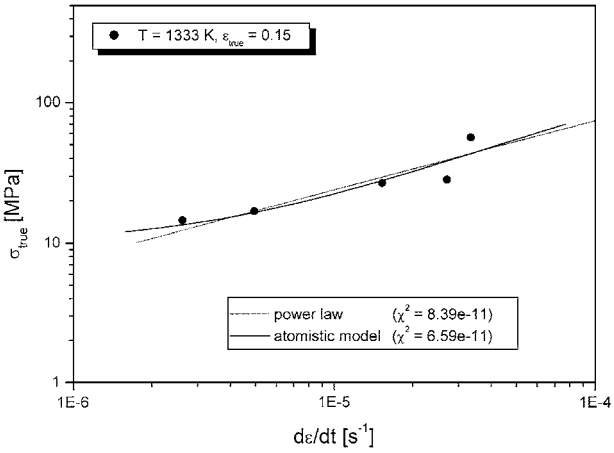

Figure 5 Double logarithmic plot of the flow stress-strain rate data at a constant true strain value of 0.15 for the n-5Y-PSZ samples tested at 1333 K. Analysis of the data was done using the two parameter power law and Equation 4.

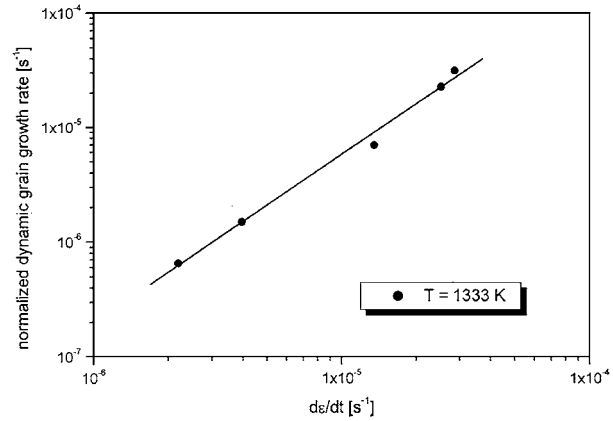

(a)

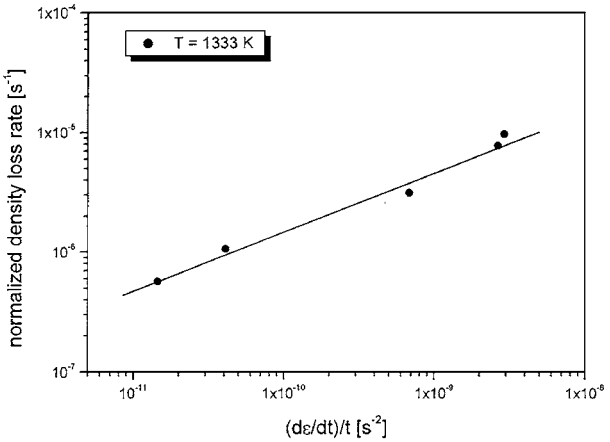

(b)

Figure 6 Phenomenological relationship between microstructural evolution and test conditions: normalized dynamic grain growth rate versus strain rate (a) and the normalized density loss rate versus strain rate divided by time (b).

with $\kappa = 0.12$ and $\varphi = 0.51$. While the division of the strain rate by time (for normalization) may be justified on the grounds that at a slower strain rate accumulation of strain in a given time and hence the effect on the density loss rate is less, it is also safe to state that other combinations of the experimental variables too may be equally successful. Further work is needed before Equation 14 can be regarded as a physically meaningful description. The high resolution SEM micrograph presented as Fig. 7 corresponds to a specimen elongated by 36% at 1333 K. The average size of the equiaxed grains after deformation was 113 nm. The dominance of grain boundary sliding, as revealed by the clear delineation of grain boundaries by deformation, is evident. Also, the surface delamination seen in the deformed specimen is very similar to what was reported by Hazzledine and Newbury [42] in a metallic superplastic alloy. Based on the present analysis of superplastic flow in a ceramic and the earlier results pertaining to metallic systems [33, 34], it is clear that a model based on grain boundary sliding controlled flow can apply equally to metallic and ceramic materials.

5.2. The results of Owen and Chokshi [13]

The experimental results of Owen and Chokshi [13] also can be understood in terms of the grain boundary sliding controlled flow model outlined in Section 2. As before, the data presented in Figs 4 and 7 of [13] (and reproduced as Fig. 1 in [14]) were analyzed using Equations 4–9 and the minimum variance unbiased estimate criterion. The findings are presented in Table I. The predicted strain rates are close to the experimentally observed values and *always* the accuracy is within an order of magnitude.

A prediction of the model (Equation 1) is that the threshold stress, σ_0, varies according to the relation, $\sigma_0 \propto \frac{1}{D^{a_2}}$, i.e., σ_0 decreases with increasing grain size. It was also stated in Section 2 that in a real material in which grain size and shape distributions are present, a_2 has to be found experimentally. Using the σ_0 values reported in Table I for the three grain sizes tested by Owen and Chokshi [13] a_2 was evaluated as 0.028. As required by the model, σ_0 decreased with increasing grain size. From Section 2c, it follows that the grain size dependence of strain rate at a given temperature should obey Equation 10. This relationship is plotted in Fig. 8. Evidently the fit is excellent. This result emphasizes the need to base arguments about atomistic mechanisms on microstructural and topological considerations, in addition to those based on simple macrolevel measurements. Here, it has been demonstrated that the grain size dependence of the strain rate in the entire experimental range employed by Owen and Chokshi [13] obeys Equation 10. Therefore, the argument [14] that the rate controlling process is Coble creep because over a limited range the grain size dependence of strain rate is inverse cubic is to be viewed with caution.

From the values of C_1 presented in Table I corresponding to a grain size of 0.41 μm and different temperatures, the activation energy for the rate controlling process was calculated using Equation 12 (Fig. 9). An activation energy value of 457 ± 135 kJ mol^{-1} was obtained. This value is close to those reported earlier by Owen and Chokshi [13] and Berbon and Langdon [14]. But their arguments are based on diffusion controlled flow models. This again highlights the danger in basing arguments about atomistic models only on macroscopic measurements like the activation energy, stress exponent and grain size dependence of flow rate.

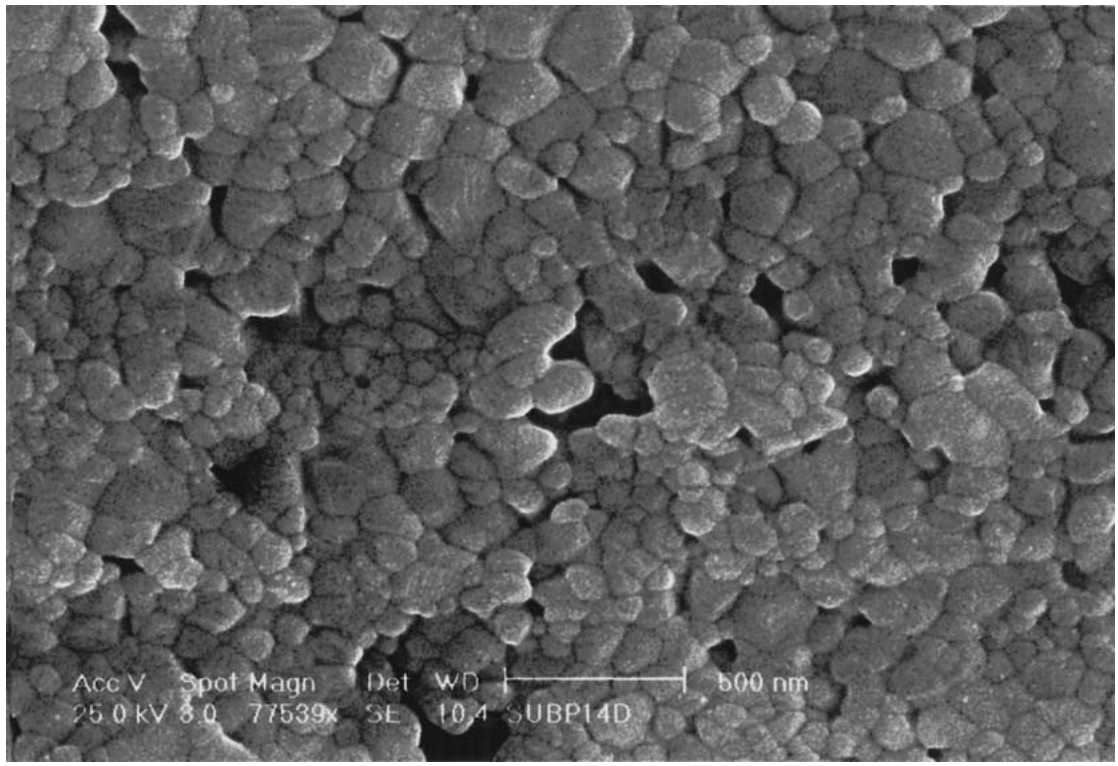

Figure 7 High resolution SEM surface image of a n-5Y-PSZ ceramic after deformation.

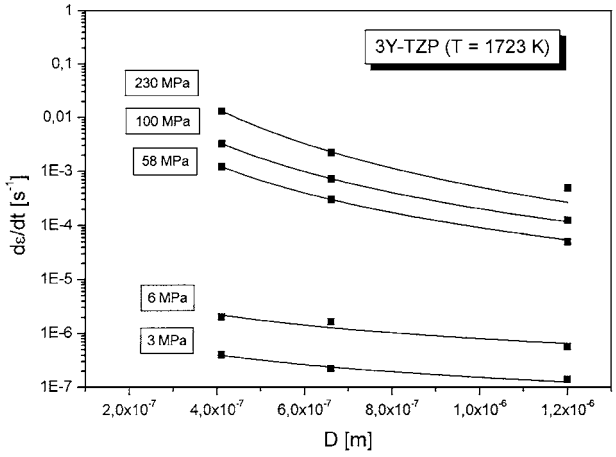

Figure 8 Logarithmic strain rate versus grain size data from [13] for 3Y-TZP at 1723 K and different stress levels. The data were fitted to Equation 10 (solid lines).

5.3. Ab initio calculations

Based on the foregoing, it can be unequivocally stated that both the experimental results of the present authors as well as those of Owen and Chokshi [13] can be understood in terms of the grain/interphase boundary sliding controlled flow model described in Section 2.2 with the aid of *three* constants. However, for making a connection with the physical model, the constants σ_0, Q (theoretically connected to ΔF_0) and C_1 values reported in Table I and Section 5(b) should be shown to be of the right order of magnitude by *ab initio* calculations.

With a_2 in Equation 1 equal to 0.028, $G = 95 \times 10^3$ MPa [14], $\gamma_B = 0.62$–0.82 Jm^{-2} [43, 44], $N = 4$ (value assumed based on experiments on Al-based superplastics [33]), grain size $D = 0.41$–1.20 μm or 50–100 nm (as the case may be), from Equation 1 a σ_0 value in the range of 0.86–1.05 MPa is predicted. This is of the right order of magnitude (see Table I) for the results of Owen and Chokshi [13], particularly because the γ_B value assumed corresponds to $ZrO_2 + 8$ mol% Y_2O_3 [43, 44] while Owen and Chokshi [13] did their experiments on $ZrO_2 + 3$ mol% Y_2O_3. Also the value of N has been assumed and not directly measured. As for the present results, the predicted value of σ_0 is less than the value determined from the experiments (Section 5a) by a factor of 10. This is attributed to the significantly lower temperatures employed here (1333 K vs. 1623–1723 K in the experiments of Owen and Chokshi [13] and the temperature range in which γ_B was measured). It is well known that G increases (approximately linearly) with decreasing temperature in the temperature range of interest and according to the grain boundary sliding controlled flow model $\sigma_0 \propto G^{0.5}$. Moreover, N, the number of contiguous grain boundaries that form the plane interface, will change with temperature. Thus, it is reasonable to state that the σ_0 values determined from the experiments are physically realistic. Further, the prediction of the model that σ_0 *increases* with *decreasing* grain size or temperature (Equation 1; see also [28, 33]) is verified (Table I). However, it is safe to note that at the present stage of development of the model, if grain size and shape distributions are present in a material, a_2 in Equation 1 can only be obtained from experiments. Also, a method of theoretically determining the value of N is yet to be suggested.

The model also enables the prediction (a) of the free energy of shear transformation resulting from the rate controlling step (Equation 3) and (b) through the relation $\Delta F_0 = Q - T\Delta S$ the activation energy for the rate controlling process. For the present calculations,

TABLE I Physical parameters and the experimental and the predicted strain rates $d\varepsilon_{exp}/dt$ and $d\varepsilon_{pred}/dt$, for the data of Owen and Chokshi [13]

3Y-TZP ($D = 1.2\,\mu$m, $T = 1723$ K)				
Physical parameters	α	C_1 [MPa^{-1} s^{-1}]	σ_0 [MPa]	σ_m [MPa]
	0.3068	1.61×10^{-6}	2.94	61
	σ_{true} [MPa]	$d\varepsilon_{exp}/dt$ [s^{-1}]	$d\varepsilon_{pred}/dt$ [s^{-1}]	
Experimental and predicted strain rates at different stress levels	3	1.4×10^{-7}	1.2×10^{-8}	
	6	5.7×10^{-7}	1.8×10^{-6}	
	16	4.1×10^{-6}	9×10^{-6}	
	59	5×10^{-5}	6×10^{-5}	
	96	1.6×10^{-4}	1.3×10^{-4}	
	215	4.9×10^{-4}	5×10^{-4}	
3Y-TZP ($D = 0.66\,\mu$m, $T = 1723$ K)				
Physical parameters	α	C_1 [MPa^{-1} s^{-1}]	σ_0 [MPa]	σ_m [MPa]
	0.2577	1.04×10^{-5}	2.96	140
	σ_{true} [MPa]	$d\varepsilon_{exp}/dt$ [s^{-1}]	$d\varepsilon_{pred}/dt$ [s^{-1}]	
Experimental and predicted strain rates at different stress levels	3	2.2×10^{-7}	8.6×10^{-7}	
	6	1.65×10^{-6}	1.4×10^{-5}	
	20	2.1×10^{-5}	9×10^{-5}	
	58	3×10^{-4}	3.3×10^{-4}	
	98	7.2×10^{-4}	6.5×10^{-4}	
	235	2.2×10^{-3}	2.2×10^{-3}	
3Y-TZP ($D = 0.41\,\mu$m, $T = 1723$ K)				
Physical parameters	α	C_1 [MPa^{-1} s^{-1}]	σ_0 [MPa]	σ_m [MPa]
	0.3359	4.61×10^{-5}	2.97	48
	σ_{true} [MPa]	$d\varepsilon_{exp}/dt$ [s^{-1}]	$d\varepsilon_{pred}/dt$ [s^{-1}]	
Experimental and predicted strain rates at different stress levels	3	4×10^{-7}	8.8×10^{-7}	
	6	2×10^{-6}	3.2×10^{-5}	
	10	9.8×10^{-6}	8.4×10^{-5}	
	16	4×10^{-5}	1.7×10^{-4}	
	30	3.1×10^{-4}	4.4×10^{-4}	
	39	7.9×10^{-4}	6.6×10^{-4}	
	58	1.2×10^{-3}	1.2×10^{-3}	
	100	3.2×10^{-3}	3×10^{-3}	
	230	1.3×10^{-2}	1.3×10^{-2}	
3Y-TZP ($D = 0.41\,\mu$m, $T = 1673$ K)				
Physical parameters	α	C_1 [MPa^{-1} s^{-1}]	σ_0 [MPa]	σ_m [MPa]
	0.3168	2.95×10^{-5}	5.92	135
	σ_{true} [MPa]	$d\varepsilon_{exp}/dt$ [s^{-1}]	$d\varepsilon_{pred}/dt$ [s^{-1}]	
Experimental and predicted strain rates at different stress levels	6	4.6×10^{-7}	8.9×10^{-7}	
	16	1.4×10^{-5}	1.2×10^{-4}	
	42	2.9×10^{-4}	4.8×10^{-4}	
	100	2×10^{-3}	1.6×10^{-3}	
	227	6×10^{-3}	5.8×10^{-3}	
3Y-TZP ($D = 0.41\,\mu$m, $T = 1623$ K)				
Physical parameters	α	C_1 [MPa^{-1} s^{-1}]	σ_0 [MPa]	σ_m [MPa]
	0.3048	6.50×10^{-6}	5.99	69
	σ_{true} [MPa]	$d\varepsilon_{exp}/dt$ [s^{-1}]	$d\varepsilon_{pred}/dt$ [s^{-1}]	
Experimental and predicted strain rates at different stress levels	6	2×10^{-7}	5.5×10^{-7}	
	20	3.9×10^{-6}	4.1×10^{-5}	
	42	8.5×10^{-5}	1.3×10^{-4}	
	100	5.4×10^{-4}	4.9×10^{-4}	
	230	2×10^{-3}	2×10^{-3}	

Poisson's ratio ρ is taken as (1/3), $G = 95 \times 10^3$ MPa [14], $V_0 = \frac{2}{3}\pi\delta^3$ with the grain boundary width $\delta = 2.5$b ($b = 0.36$ nm [14]), $\gamma_0 = 0.1$ (bubble raft experiments [45]) and $\varepsilon_0 = (\gamma_0/2)$. Then, a ΔF_0 value of 486.5 kJ mol^{-1} is predicted. For high temperature phenomena, e.g., diffusion, $\exp(\Delta S/R) \cong 12$ [46]. Assuming that the entropy of activation for the grain boundary sliding process is of the same order as that for diffusion, an activation energy, Q, for the rate controlling grain/interphase boundary sliding process of 521 kJ mol^{-1} is predicted ($T\,\Delta S = 34.5$ kJ/mol.). This compares favorably with an activation energy value of 457 ± 135 kJ mol^{-1} determined experimentally for the data for Owen and Chokshi [13] - Fig. 9. Recently, the activation energy for the rate controlling process in the compressive deformation of n-5Y-PSZ in the temperature range of 1363 K–1503 K has been reported to be $Q = 507 \pm 14$ kJ mol^{-1} [47]. Evidently, that value is very close to the theoretical and the experimental values reported here.

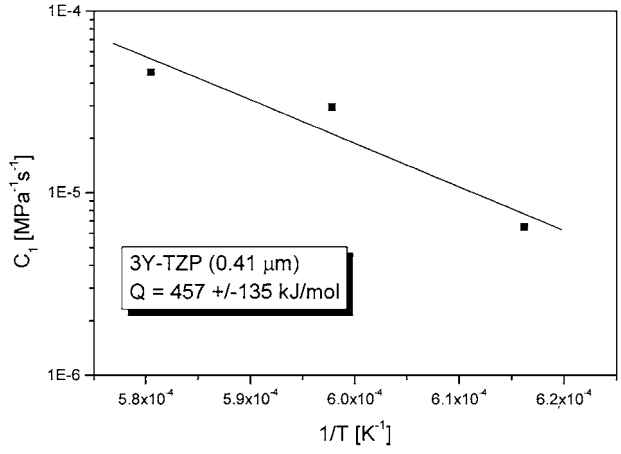

Figure 9 Arrhenius plot of the physical parameter C_1 against the inverse temperature for 3Y-TZP with an initial grain size of 0.41 μm (data from [13]).

Finally, it is also possible to predict the value of C_1 (Equation 6) *ab initio*. Taking $\delta = 2.5\,b (b = 0.36$ nm), $D = 0.055$–$1.2\,\mu$m, $\gamma_0 = 0.1$, $V_0 = (2/3)\pi\delta^3$, $\omega_0 = (kT/h)\exp(-\Delta F_0/kT)$ with $\Delta F_0 = 486.5$ kJ mol^{-1} and $h = 6.625 \times 10^{-36}$ J.s, a C_1 value in the range of 6.7×10^{-7}–7×10^{-8} s^{-1} MPa^{-1} is predicted. Here, the values of δ, γ_0 and ΔF_0 are assumed. Less than 10% variation in these values, will easily allow even an exact matching with the C_1 values obtained experimentally.

6. Conclusions

Based on the present investigation, the following conclusions are drawn:

1. Partially stabilized $ZrO_2 + 5$ mol% Y_2O_3 ceramic of average grain size 54 nm could be subjected to steady state deformation and a true strain of 0.08 at as low a temperature as 1283 K ($0.42T_m$).

2. At a relatively low temperature of 1403 K ($0.46T_m$) a specimen of average grain size 75 nm could be elongated by 70% in uniaxial tension.

3. Equiaxed grains and clearly delineated grain boundaries in deformed nanocrystalline samples, as revealed by scanning electron microscopy, provided clear evidence for the occurrence of significant grain boundary sliding.

4. Both static and dynamic grain growth were present in the nanocrystalline specimens. Exposure to test temperature without deformation for the duration of a

tensile test led to densification of the sample. In contrast, the relative density of a specimen decreased with increasing deformation.

5. The present results as well as those of Owen and Chokshi [13] could be explained using the grain boundary sliding controlled flow model due to Padmanabhan and Schlipf [28] originally proposed for microcrystalline materials. *At the level of phenomenology*, a *quantitative explanation* for optimal structural superplasticity could be presented with the aid of *3 material-dependent constants*. If the grain size is uniform and the grain shape is of simple geometry, e.g., a rhombic dodecahedron, the only input required through a *superplasticity experiment* is the number, N, of grain boundaries that join to form a plane interface during the occurrence of mesoscopic (cooperative) boundary sliding. (All other material properties like shear modulus, Poisson's ratio, grain boundary energy, grain boundary width and the mean strain associated with a unit shear event are to be taken from literature or obtained in general experiments not necessarily related to superplastic flow.) If grain size and shape distributions are present in a material, the grain size exponent in the relationship $\sigma_0 \propto \frac{1}{L^{a_2}}$ also has to be obtained experimentally. Thus, in real materials at the level of atomistics, two superplasticity experiments are necessary to determine N and a_2. Then, the stress-strain rate behavior can be predicted for the entire optimal range.

6. The approach adopted in this paper has the advantage that structural superplasticity in both metallic and ceramic superplastics having micro-, sub-micro- and nano-crystalline grains can be understood on a common basis.

Acknowledgement

The authors thank the Deutsche Forschungsgemeinschaft (DFG) for sponsoring this work. KAP thanks the '2 + 2' program of the Department of Science and Technology, Government of India and the BMBF, Germany, and the Alexander von Humboldt Foundation, Bonn, for enabling him to participate in some experiments at the Darmstadt University of Technology, Germany. UB is grateful to the Deutsche Akademischer Austauschdienst (DAAD) for financially supporting his visit to IIT Kanpur.

References

1. K. A. PADMANABHAN and G. J. DAVIES, "Superplasticity" (Springer Verlag, Heidelberg-Berlin-New York, 1980).
2. O. A. KAIBYSHEV, "Superplasticity in Alloys, Intermetallides and Ceramics" (Springer Verlag, Berlin, 1992).
3. T. G. NIEH, J. WADSWORTH and O. D. SHERBY, "Superplasticity in Metals and Ceramics" (Cambridge University Press, 1997).
4. F. WAKAI, S. SAKAGUCHI and Y. MATSUNO, *Adv. Ceram. Mater.* **1** (1986) 259.
5. F. WAKAI and H. KATO, *ibid.* **3** (1988) 71.
6. T. G. LANGDON, *JOM* **42**(7) (1990) 8.
7. F. WAKAI, *Acta Metall. Mater.* **42** (1994) 1163.
8. S. PRIMDAHL, A. THOELEN and T. G. LANGDON, *ibid.* **43** (1995) 1211.
9. J. A. HINES, Y. IKUHARA, A. H. CHOKSHI and T. SAKUMA, *Acta Mater.* **46** (1998) 5557.
10. F. WAKAI, in Proc. MRS Int. Meeting on Advanced Materials, edited by M. Doyama, S. Somiya and R. P. H. Chang, Vol. 7, MRS, Pittsburgh, Pa. (1989) p. 225.
11. M. NAUER and C. CARRY, in "Euro-Ceramics," edited by G. de With, R. A. Terpstra and R. Metselaar, Vol. 3 (Elsevier Applied Science, London, 1989) p. 323.
12. J. YE, A. DOMINGUEZ-RODRIGUEZ, R. E. MEDRANO and O. A. RUANO, in Third Euro-Ceramics, edited by P. Duran and J. F. Fernandez, Vol. 3 (Faenza Editrice Iberica, Castellon de la Plana, Spain, 1993) p. 525.
13. D. M. OWEN and A. H. CHOKSHI, *Acta Mater.* **46** (1998) 667.
14. M. Z. BERBON and T. G. LANGDON, *ibid.* **47** (1999) 2485.
15. K. A. PADMANABHAN, Ph.D. Thesis, University of Cambridge, U.K., 1971.
16. *Idem.*, *Mater. Sci. Eng.* **29** (1977) 1.
17. *Idem.*, *ibid.* **40** (1979) 285.
18. J. W. EDINGTON, K. N. MELTON and C. P. CUTLER, *Prog. Mater. Sci.* **21** (1976) 61.
19. R. C. GIFKINS and T. G. LANGDON, *Mater. Sci. Eng.* **36** (1978) 27.
20. *Idem.*, *ibid.* **40** (1979) 293.
21. K. N. MELTON and J. W. EDINGTON, *Metal Sci.* **17** (1983) 408.
22. R. Z. VALIEV and T. G. LANGDON, *Acta Metall. Mater.* **41** (1993) 949.
23. H. HAHN and K. A. PADMANABHAN, *Phil. Mag.* **76B** (1997) 559.
24. H. HAHN, P. MONDAL and K. A. PADMANABHAN, *Nanostructured Materials* **9** (1997) 603.
25. K. A. PADMANABHAN, *J. Metastable and Nanocrystalline Materials* **8** (2000) 753.
26. M. V. SPEIGHT, *Acta Metall.* **23** (1975) 779.
27. *Idem.*, *Scr. Metall.* **10** (1976) 163.
28. K. A. PADMANABHAN and J. SCHLIPF, *Mater. Sci. Technol.* **12** (1996) 391.
29. W. BEERE, *J. Mater. Sci.* **12** (1977) 209.
30. O. ENGLER, K. A. PADMANABHAN and K. LÜCKE, *Modelling and Simulation in Mater. Sci. Eng.* **8** (2000) 477.
31. V. V. ASTANIN, S. N. FAIZOVA and K. A. PADMANABHAN, *Mater. Sci. Technol.* **12** (1996) 489.
32. V. V. ASTANIN, K. A. PADMANABHAN and S. S. BHATTACHARYA, *ibid.* **12** (1996) 545.
33. T. A. VENKATESH, S. S. BHATTACHARYA, K. A. PADMANABHAN and J. SCHLIPF, *ibid.* **12** (1996) 635.
34. F. U. ENIKEEV, K. A. PADMANABHAN and S. S. BHATTACHARYA, *ibid.* **15** (1999) 637.
35. D. WOLF, *Acta Metall. Mater.* **38** (1990) 781, 791.
36. H. HAHN, *NanoStruct. Mat.* **9** (1997) 3.
37. J. R. SEIDENSTICKER and M. J. MAYO, *Scripta Mat.* **38** (1998) 1091.
38. M. A. CLARKE and T. H. ALDEN, *Acta Met.* **21** (1973) 1195.
39. D. S. WILKINSON and C. H. CACERES, *ibid.* **32** (1984) 1335.
40. D. J. SHERWOOD and C. H. HAMILTON, *Scripta Mat.* **25** (1991) 2873.
41. B. N. KIM, K. H. HIRAGA, Y. SAKKA and B. W. AHN, *Acta Mat.* **47**(12) (1999) 3433.
42. P. M. HAZZLEDINE and D. E. NEWBURY, "Grain Boundary Structure and Properties," edited by G. A. Chadwick and D. A. Smith (Academic Press, London, 1976) p. 235.
43. TSOGA and P. NIKOLOPOULOS, *J. Mater. Sci.* **31** (1996) 5409.
44. R. CHAIM, A. H. HEUER and D. G. BRANDON, *J. Amer. Ceram. Soc.* **69** (1986) 243.
45. A. S. ARGON, *Acta Metall.* **27** (1979) 47.
46. A. H. COTTRELL, "Theoretical Structural Metallurgy" (The English Language Book Society and Edward Arnold (Publishers) Ltd, London, 1964) p. 182.
47. U. BETZ, Ph.D. Thesis, Darmstadt University of Technology, Germany, 2000.

Received 30 October 2000
and accepted 19 July 2001